International Journal of Heat and Mass Transfer 201 (2023) 123643

Contents lists available at ScienceDirect

International Journal of Heat and Mass Transfer

journal homepage: www.elsevier.com/locate/hmt

Dual effects of hetero-interfaces on phonon thermal transport across graphene/C_3N lateral superlattices

Xin Wu[a], Penghua Ying[b], Chunlei Li[a,*], Qiang Han[a,*]

[a] Department of Engineering Mechanics, School of Civil Engineering and Transportation, South China University of Technology, Guangzhou, Guangdong Province 510640, PR China
[b] School of Science, Harbin Institute of Technology, Shenzhen, Guangdong Province 518055, PR China

ARTICLE INFO

Article history:
Received 28 September 2022
Revised 23 October 2022
Accepted 6 November 2022

Keywords:
Graphene/C_3N lateral superlattice
Hetero-interface
Coherent phonon transport
Thermal conductivity

ABSTRACT

Two-dimensional (2D) lateral superlattices, a typical artificial nano-phononic crystal, have stimulated widespread interests and potential application prospects in terms of their physically interesting features. Herein, we have found wave-particle crossover of phonon transport in the graphene (Gr)/2D polyaniline (C_3N) lateral superlattices, which is an indication of a transition in the phonon transport mechanism from the incoherent to coherent regime. Due to the high structural similarity of C_3N to Gr, the thermal conductivity of the Gr/C_3N lateral superlattice can achieve an ultra-wide modulation range of about 500 ~ 1100 W m^{-1} K^{-1}, which is far beyond that of other superlattices. The analysis shows that an increase of the interface density will on the one hand weaken the thermal conductivity by increasing phonon-interface scattering, and on the other hand increase it by lowering the phonon transport barriers and allowing more long-wavelength phonons to participate in the transport. This determines the parabolic trend of thermal conductivity containing the minimum, and also reflects the dual effects of hetero-interfaces on phonon thermal transport. In addition, phonon calculations show that the above variation in thermal conductivity is entirely attributable to differences in the phonon mean free path for different interface densities and is not related to their group velocity.

1. Introduction

From the eternal problem of food and clothing, to the invention of the steam engine that opened up the industrial era in the past thousand years, to the epoch-making development of the microelectronics industry in the past hundred years, heat-related issues have been a powerful thread running through the history of mankind for thousands of years. At present, nanotechnology is a multidisciplinary cross-integration that has provided a powerful impetus for innovation in many fundamental disciplines such as physics, materials, and even life sciences, and has become an important source of transformative research and production [1–4]. At the same time, the development of nanotechnology makes the devices further densified and miniaturized, which will inevitably lead to the difficult problem of high local thermal energy density and difficult dissipation of waste heat, particularly in the semiconductor industry [5].

Phonons, quasi-particles excited collectively by the lattice in solids, occupy a pivotal position in the problem of thermal transport in non-metallic solid materials, represented by semiconductors [6–9]. The broad "constitutive relationship", reflecting the relationship between the structure of the study object and its properties, aims to use physics as a bridge from structural design to reliable performance modulation. Artificial phononic crystals are a typical class of functional materials guided by "constitutive relationships", where the periodic design of the structure enables the modulation of acoustic or elastic waves, or even heat transfer in solids [10–14]. Superlattices, formed by the alternating periodic arrangement of two or more different materials, were the first nanoscale phononic crystals to be investigated, starting around the end of the 1970's [15]. In this way, the structural design by phononic crystals represented by superlattices holds great promise for the modulation of thermal transport properties in nanoscale materials, which is indeed the case.

In superlattices with characteristic dimensions at the nanoscale, the different manifestations of transport states caused by the traits of phonon wave-particle crossover are a key and interesting point of study. Since the establishment of a theoretical framework for describing the minimum thermal conductivity in superlattices, the study of thermal transport in different dimensional classes of superlattices has continued to evolve. These

* Corresponding authors.
E-mail addresses: lichunlei@scut.edu.cn (C. Li), emqhan@scut.edu.cn (Q. Han).

https://doi.org/10.1016/j.ijheatmasstransfer.2022.123643
0017-9310/

Table 1
Structural information on Gr/C_3N lateral superlattices with different periodic properties.

	Number of periods	Period length (nm)	Interface density (nm^{-1})	Number of atoms
G_1	1	25.920	0.077	9600
G_2	2	12.960	0.154	9600
G_3	6	4.320	0.463	9600
G_4	10	2.592	0.772	9600
G_5	15	1.728	1.157	9600
G_6	30	0.864	2.315	9600

studies include quasi-one-dimensional Si/Ge nanowire superlattices [16–19], two-dimensional (2D) heterostructures [20–22] represented by graphene (Gr)/hexagonal boron nitride (h-BN) superlattice nanoribbons [23], as well as near-blocky AlAs/GaAs superlattices [24] and 2D van der Waals superlattices represented by Gr/h-BN [25,26]. They also cover different perspectives from theoretical calculations to experimental validations to simulations. Specifically, the coherence-related regime modulation of phonon transport has been further characterized by novel results on the thermal conductivity, which imply a significant advance towards the goal of phonon manipulation. However, superlattices composed of widely favored 2D materials as components are relatively poorly researched in this field, with a notable gap in particular around graphene and its analogues. Since the successful preparation of two-dimensional polyaniline (C_3N) in the laboratory, a 2D material with the hexagonal honeycomb lattice similar to that of graphene, it has attracted a great deal of academic attention [27–29]. The similar lattice constant to graphene create extremely favorable conditions for the formation of lateral heterostructures, which also provide the necessary guarantees for the construction of superlattices with both as basic components. Due to the high structural similarity, C_3N can even be regarded as a product of graphene doped with nitrogen atoms in a regular manner from the composition. The thermal resistance of the Gr/C_3N lateral heterostructures [30,31] is much lower than that of the heterostructures formed by Gr and other 2D materials such as h-BN [32,33] and silicene [34]. Therefore, clarifying the behavior of phonon thermal transport in superlattices composed of Gr and C_3N can help to provide further insight into the influence of one-dimensional interfaces on the coherence of phonon transport and the macroscopic modulation of thermal conductivity in 2D systems.

In the present work, we report on the interesting phonon thermal transport behavior induced by transport regime transitions in Gr/C_3N lateral superlattices. The specific influence of the interface density or period length on the thermal transport across the hetero-interface in the superlattice is explored through extensive molecular dynamics (MD) simulations as well as lattice dynamics-based phonon calculations. Based on the refinement of the analysis of thermal conductivity to the different directions of phonons and the contribution of different frequency bands, a useful analysis of the physical mechanisms associated with the phenomenon of thermal conductivity variation at the phonon level is presented.

2. Model and methods

Herein, six Gr/C_3N lateral superlattices with different period lengths are constructed, with the parameter details shown in Table 1. Among them, the period length is a key structural feature control parameter of the superlattices, which directly and comprehensively reflects the periodic properties of the structures. In addition, the interface density, another structural characteristic parameter inversely proportional to the period length, is more focused on describing the structural characteristics of the superlattice from the perspective of the hetero-interface. Three of these superlattices, G_2, G_3, and G_4, are represented in Fig. 1 (see Fig. S1 for all six in the Supplementary Information (SI)), all with an overall size of approximately 25.92 nm × 9.98 nm, based on structural information determined by rigorous size effect verification, which will be described in detail subsequently. It should be noted here that for superlattices with different period lengths, the models contain different numbers of cell units along the thermal transport direction (y-axis), i.e. the number of periods, in order to avoid as much as possible the differential influence of size effects on the different models.

All molecular dynamics (MD) simulations and lattice dynamics calculations in this work have been implemented based on the Graphical Processing Unit Molecular Dynamics (GPUMD) software package [35–38], an efficient tool that has been widely used in MD simulations including thermal transport. The C–C and C–N interactions present in the system are described by the optimized Tersoff potential [39,40], a set of potential functions that are reliable for the study of thermal transport in graphene and carbon nitride systems. In addition, to ensure optimal system stability and energy convergence, a time step of 0.5 fs was used for all simulations in this study. At the beginning of each individual simulation, the same thermal equilibration steps are performed as follows: first the atoms are given an initial velocity matching the system temperature of 10 K and equilibrated at zero pressure for 1 ns; subsequently they are heated to a target temperature of 300 K for the next 1 ns; and finally the NPT equilibration is continued at that condition for 1 ns. After the thermal equilibrium process is completed, different specific output processes will be executed based on different simulation methods. The overall idea of the MD calculations in this paper is to use homogeneous non-equilibrium molecular dynamics (HNEMD) and its spectral decomposition (SHC) method as the main tool for thermal conductivity assessment, and to supplement it with non-equilibrium molecular dynamics (NEMD) and its SHC method for the associated phonon analysis. (Please see SI for more details of the computational methods and data processing) In addition to MD simuations, the lattice dynamics calculations were also implemented to obtain the phonon dispersions and corresponding group velocity of different superlattices.

3. Results and discussion

First of all, it is necessary to explain the details and the specific configurations in the calculation process, which is the guarantee for the reliability of the results. As presented in the SI, the selection of the driving force parameter in the HNEMD method is a decisive indicator of whether the thermal conductivity results converge or not. Specifically, as shown in Fig. S2(a), when the strength of the driving force parameter is insufficient, the signal-to-noise ratio is too low and the data fluctuates excessively. Conversely, the system will fail to achieve the desired linear response. Furthermore, the verification of the size effect in the width direction in Fig. S3 illustrates that the thermal conductivity of the system along the length direction is not sensitive to the width, where periodic boundary conditions are taken along the width direction. Therefore, for the HNEMD simulations, the driving force parameter of

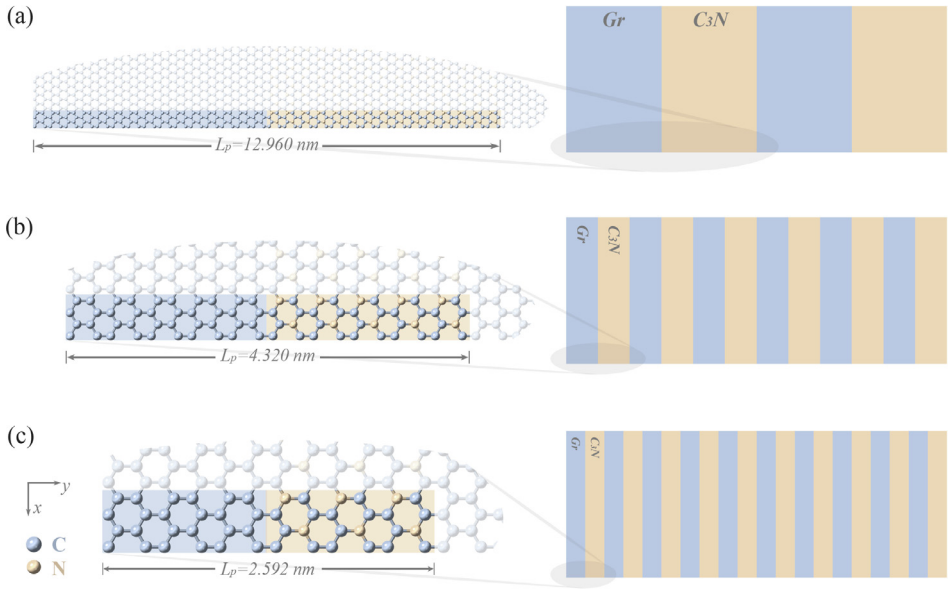

Fig. 1. Schematic structures of three representative Gr/C_3N lateral superlattices (a) G_2, (b) G_3, and (c) G_4 with period lengths of 12.96 nm, 4.32 nm, and 2.592 nm, respectively. The right side is used to illustrate the overall structure of the superlattice, which has an overall size of approximately 25.92 $nm \times 9.98$ nm. The left side is a schematic representation of the respective corresponding atomic-level local enlargements within a mono-period, where the colored shaded areas indicate the cell units of the superlattice. (See supplementary information for the schematic structures of other superlattices).

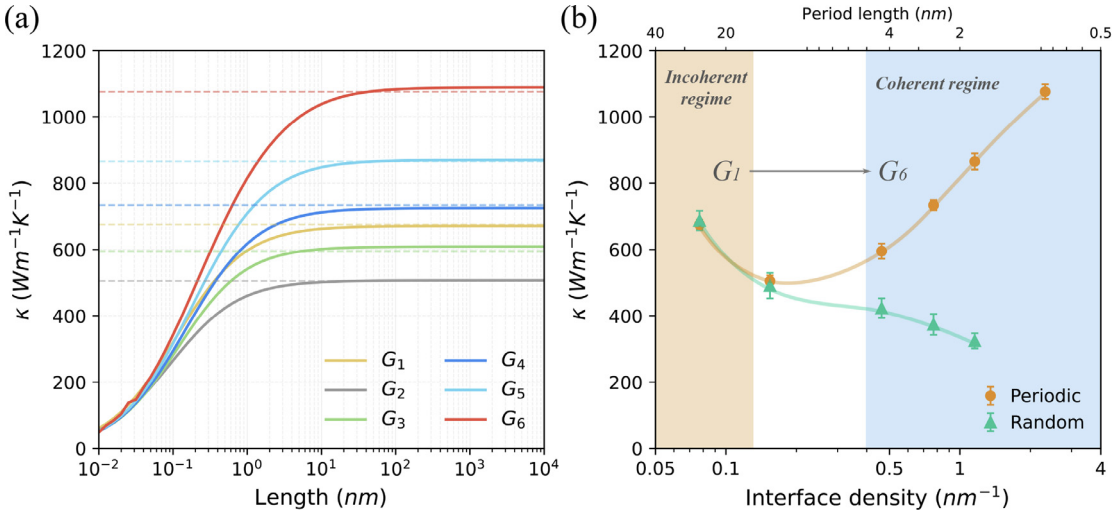

Fig. 2. Calculated thermal conductivity of the Gr/C_3N superlattices. (a) The variation of the thermal conductivity of the superlattices $G_1 \sim G_6$ with the length of the system as calculated by the SHC method, where the different horizontal dotted lines correspond to the HNEMD calculation results, which are in high agreement. (b) Thermal conductivity of the superlattice as a function of its interface density or period length. The green triangular data indicate the thermal conductivity of the random superlattice, which corresponds to the contribution of incoherent phonons. (For interpretation of the references to color in this figure legend, the reader is referred to the web version of this article.)

$F_e = 0.5$ μm^{-1} was chosen in this study and nine independent simulations were performed for each model and averaged as the final thermal conductivity results. For the NEMD method, as shown in Fig. S4, a heat bath region of sufficient size (about 10 nm) is set up to ensure that phonons entering the heat bath region do not return again into the effective heat transfer area [41,42].

Here, the thermal conductivity of Gr/C_3N superlattices $G_1 \sim G_6$ along the y-direction is investigated by the HNEMD and NEMD and their SHC methods, with the interface density as the main independent variable. As shown in Fig. 2(a), the thermal conductivity results for the infinitely long system obtained by both SHC and HNEMD methods are highly consistent for each superlattice, which further ensures the reliability of the results. From Fig. 2(b), it can be observed that the thermal conductivity of the Gr/C_3N superlattices shows a parabolic trend of decreasing followed by increasing with increasing interface density, which is similar to the results exhibited in other similar superlattice systems. It is worth noting that the range of thermal conductivity variation for superlattice systems including quasi-one dimensional and bulk is essentially concentrated in the range of $0 \sim 30$ W m^{-1} K^{-1} [17,25], and even for the Gr/h-BN lateral superlattice in the same 2D system, the thermal conductivity varies over a range of only $80 \sim 160$ W m^{-1} K^{-1} [23]. The Gr/C_3N superlattice thermal conductivity in this study, however, is able to reach a range of variation of about $500 \sim 1100$ W m^{-1} K^{-1}, which also implies the possibility of its very large range of modulation applications.

This non-monotonic variation in thermal conductivity depending on the interface density is mainly attributed to a shift in the phonon transport regime, specifically the difference between the presence and absence of the coherence. In the Gr/C_3N superlattice,

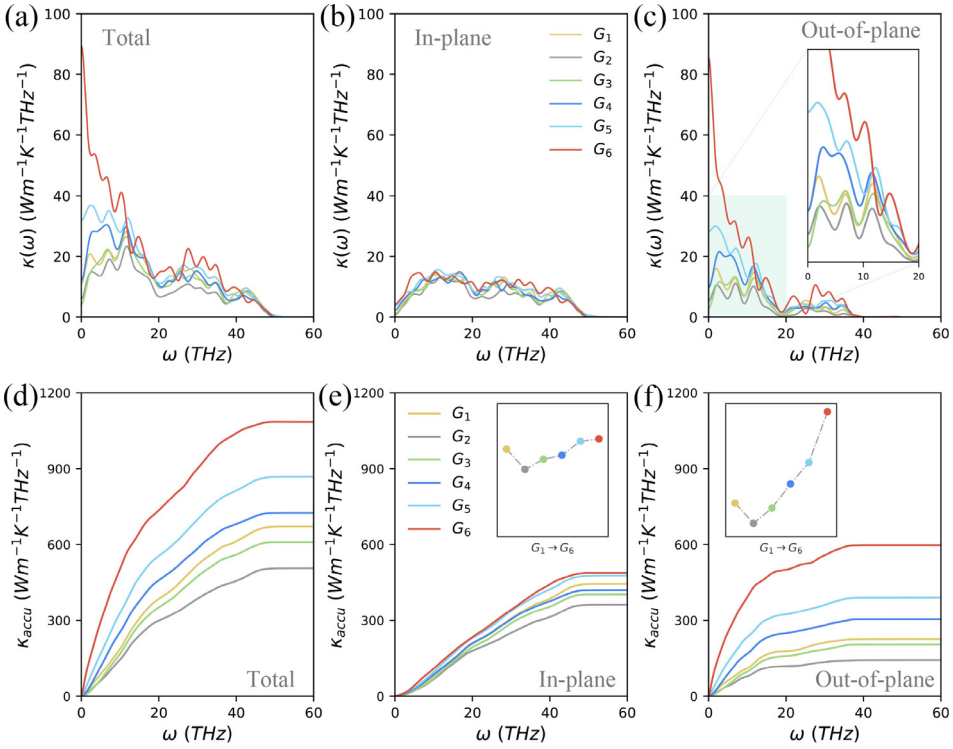

Fig. 3. The (a) spectral thermal conductivity results for the Gr/C_3N superlattice $G_1 \sim G_6$ and its (b) in-plane and (c) out-of-plane components, and the corresponding (d–f) cumulative values of thermal conductivity as a function of phonon frequency. The subplot in (c) represents a magnified display of the $0 \sim 20$ THz frequency band, which is the core component leading to the differentiation of thermal conductivity. The subplots in (e) and (f) show the in-plane and out-of-plane contributions for thermal conductivity of the six superlattices, respectively, both of which have exactly the same range of values in order to perform a clear comparison.

the hetero-interface is undoubtedly the main source of phonon scattering, yet as the interface density increases, an increase in thermal conductivity occurs that is contrary to the enhanced effect of phonon scattering. Therefore, while keeping the number of hetero-interfaces constant, we break the perfect periodicity of the superlattice by randomly adjusting the size of its components, which we call as “random superlattice”. The random superlattice is able to ensure phonon scattering at interfaces as close as possible by controlling the number of hetero-interfaces, and to suppress coherent transport of phonons by breaking the periodicity, forming together with the superlattice an ideal system for the study of coherence-dependent phonon transport regimes. Fig. S6 shows the structure of the partially random superlattice $RG_1 \sim RG_6$ corresponding to the superlattice $G_1 \sim G_5$. Note here that since the superlattice G_6 contains the smallest unit of Gr and C_3N in a single period, i.e. a single hexagonal ring, the structure at this interface density is unique and has no variants, so the random superlattice RG_6 does not exist. For each random superlattice, we created 12 different structures and calculated their thermal conductivity, as shown in the green triangle in Fig. 2(b). The thermal conductivity of the random superlattice continues to decrease as the interface density increases, due to the stronger phonon scattering caused by the increased hetero-interface density. Next, the thermal conductivity results for the superlattice and the random superlattice are compared longitudinally. At low interface densities, their thermal conductivities are almost equal, reflecting the fully incoherent phonon transport properties where the thermal conductivity is affected by approximately the same hetero-interface scattering. However, as the interface density increases, the two show opposite trends. The thermal conductivity of the superlattice appears to be partially contributed by coherently transported phonons and progressively more coherent, as reflected in the difference between its thermal conductivity and that of the random superlattice. Overall, the incoherent phonon-dominated thermal conductivity of the superlattice gradually decreases as the interface density increases, while the coherent phonon-dominated thermal conductivity increases from absent to present and continues to increase, together leading to a decreasing and then increasing trend in the thermal conductivity of the Gr/C_3N superlattice, which is a macroscopic manifestation of the transition from the incoherent to the coherent regime of phonon transport. In addition, the calculated thermal conductivity results for a Gr/C_3N superlattice with an extended period length to about 100 nm and an interface density to about 0.02 nm^{-1} are also shown in Fig. S7, which provides a meaningful extension of the thermal conductivity results for the incoherent transport regime in Fig. 2(b). It is also important to mention that in the absence of the hetero-interfaces, that is, pristine graphene and C_3N, the thermal conductivity are beyond 2000 W m^{-1} K^{-1} [36,43], which is significantly higher than that of the Gr/C_3N superlattice. This is a natural consequence of the introduction of the hetero-interfaces.

Next, to further explore the deeper reasons for the difference in thermal conductivity of the superlattices $G_1 \sim G_6$, their spectral thermal conductivity results $\kappa(\omega)$ with respect to phonon frequencies are plotted in Fig. 3(a–c). Firstly, from an overall perspective, the contribution of superlattice thermal conductivity comes from phonons in the low-and-mid frequency bands between 0 and 40 THz, with the low frequency phonons at $0 \sim 20$ THz clearly dominating. Moreover, the difference between the thermal conductivity of the superlattice $G_1 \sim G_6$ in the mid-frequency band is not significant compared to the low-frequency band, which reinforces that the contribution of low-frequency phonons to the thermal conductivity is the fundamental reason for the differentiated thermal conductivity results. As can be seen in Fig. 3(b), the in-plane phonon contribution component of the six superlattice thermal conductivities is almost indistinguishable both in terms

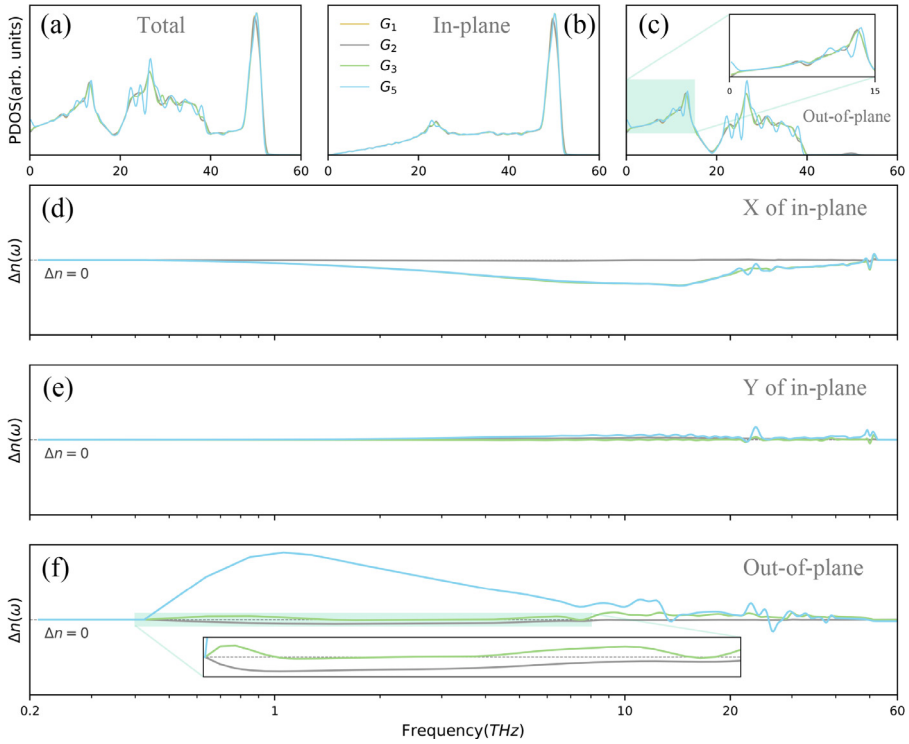

Fig. 4. Variation of (a) phonon density of states and their (b) in-plane and (c) out-of-plane components with phonon frequency for Gr/C_3N superlattices G_1, G_2, G_3, and G_5. (d–f) With G_1 as a reference system, the relative phonon populations of G_2, G_3, and G_5 as a function of phonon frequency, which includes the components in the three directions in the Cartesian coordinate system.

of amplitude and dominant frequency band, and the thermal conductivity contributions in the mid frequencies are almost all derived from in-plane phonons. However, the results for the out-of-plane phonon contribution to the spectral thermal conductivity in Fig. 3(c) exhibit a very similar shape to the total $\kappa(\omega)$. Specifically, the difference in the low-frequency out-of-plane phonon contribution to the thermal conductivity is directly responsible for the difference in the thermal conductivity of the superlattice at different interface densities. During the transition from the incoherent to the coherent transport regime, the low-frequency out-of-plane part of the $\kappa(\omega)$ exhibits the same suppressed and then enhanced trend as the thermal conductivity change in Fig. 2(b). In the incoherent transport regime, the increase in superlattice interface density suppresses the contribution of low-frequency out-of-plane phonons to the thermal conductivity by increasing the phonon scattering rate. Entering the coherent transport regime, the increasing superlattice interface density instead continuously excites the low-frequency out-of-plane phonon contribution, resulting in an unexpected and sustained increase in thermal conductivity.

Also as shown in Fig. S8, comparing the spectral thermal conductivity results for pristine graphene in Ref. [44], the shape and trend of the superlattice spectral thermal conductivity becomes increasingly close to that of pristine graphene as coherent transport is enhanced within the coherent transport regime, implying a similar phonon state. In other words, the high interface density of the superlattice greatly weakens the hybrid effect through the realization of coherent transport, which is beneficial for the application of lateral superlattice devices in thermal transport. Further, the cumulative thermal conductivity κ_{accu} of the superlattice $G_1 \sim G_6$ with phonon frequency as the independent variable is plotted based on the spectral thermal conductivity results, as shown in Fig. 3(d–f), which enables a dynamic view of the overall results for phonon thermal conductivity over the full frequency band. In general, the difference between the in-plane phonon contribution for different superlattice thermal conductivities is small compared to that of the out-of-plane phonon, as reflected by the denseness of the κ_{accu} curve distribution. Specifically, the subplots of Fig. 3(e and f) clearly present the specific variation of the in-plane and out-of-plane components for different superlattice thermal conductivities. In particular, the out-of-plane component perfectly matches the trend of the total thermal conductivity, which further explains its dominance.

Next, we present a series of analyses of the above thermal conductivity trends of the superlattice from the perspective of phonon activity, which is an effective means of exploring its fundamental physical origin. First, the phonon density of states (PDOS), which reflects phonon activity in different modes [45,46], is calculated as shown in Fig. 4(a–c), which is obtained from an auto-correlation analysis of the atomic velocities:

$$PDOS_{i\alpha}(\omega) = \int_{-\infty}^{+\infty} \langle v_{i\alpha}(t) v_{i\alpha}(0) \rangle e^{-2\pi i \omega t} dt \quad (\alpha = x, y, z) \tag{1}$$

where $\langle v_{i\alpha}(t) v_{i\alpha}(0) \rangle$ denotes the velocity auto-correlation function (VACF) of atom i in the α direction at the time t. It should be noted that for clarity and brevity of presentation, four superlattices G_1, G_2, G_3, and G_5 are chosen here for representative analysis, and these are sufficient to capture the overall trend of the thermal conductivity variation with the interface density. A decomposition of the in-plane and out-plane contributions was also carried out, in the same way as the previous decomposition of the thermal conductivity. From Fig. 4(c), it is easy to see that among the four superlattices, the difference in the low-frequency out-of-plane phonon PDOS that dominates the difference in thermal conductivity is not obvious, except for G_5, which has a naked eye advantage. Therefore, we choose to take the PDOS of G_1 as a benchmark and introduce the following phonon mode occupation ratio $\Delta n(\omega)$ to

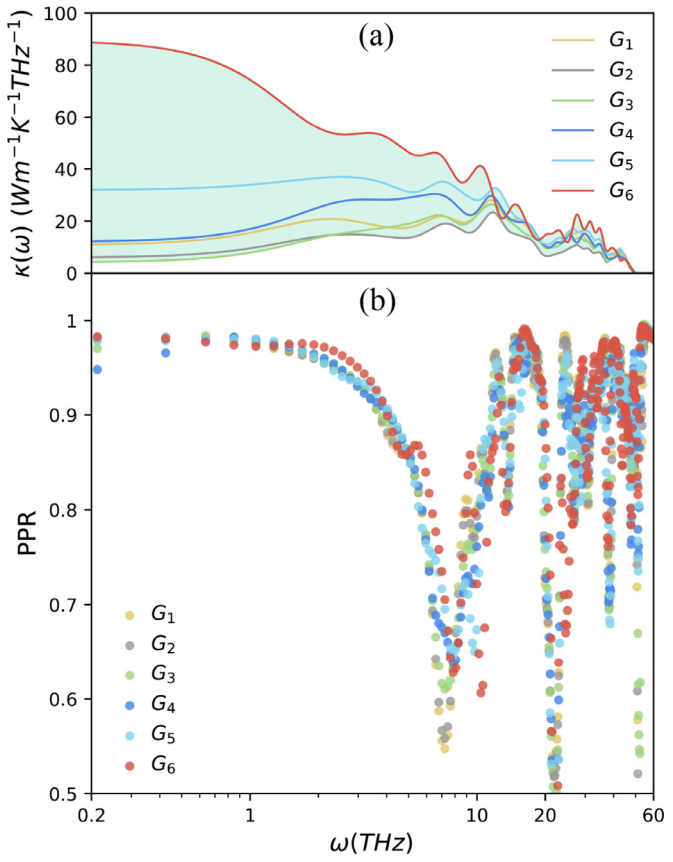

Fig. 5. (a) Variation of the spectral thermal conductivity of the Gr/C_3N superlattice $G_1 \sim G_6$ as a function of phonon frequency, where the green shading is to more graphically represent the overall difference in the thermal conductivity of the superlattice at different phonon frequency bands. (b) Phonon participation rate of the superlattice $G_1 \sim G_6$ as a function of phonon frequency. (For interpretation of the references to color in this figure legend, the reader is referred to the web version of this article.)

reflect the variation in phonon populations:

$$\Delta n(\omega) = \frac{1+\int_0^{\omega} PDOS_{EGm}d\omega'}{1+\int_0^{\omega} PDOS_{EG_1}d\omega'} - 1 \quad (m = 2, 3, 5) \tag{2}$$

The variation of the phonon populations in the superlattice with respect to G_1 can be reflected from the positive or negative of this indicator $\Delta n(\omega)$. In the direction along the thermal transport, as shown in Fig. 4(e), the in-plane phonon mode occupancy ratios of the four superlattices are almost identical. The low-frequency out-of-plane phonons that dominate the thermal transport in Fig. 4(f) show a good agreement with their thermal conductivity results: this is evident in the slightly smaller in G_2, the slightly larger in G_3, and the much larger in G_5 phonon occupancy ratios.

In addition, the effect of phonon localization on thermal transport in hybrid systems containing interfaces or defects is well worth considering, as reflected by the phonon participation rate (PPR):

$$PPR(\omega) = \frac{1}{N}\frac{\left(\sum_i PDOS_i^2(\omega)\right)^2}{\sum_i PDOS_i^4(\omega)} \tag{3}$$

where N is the total number of atoms involved in the calculation and $PDOS_i(\omega)$ is the phonon density of states result for the atom numbered i calculated from Eq. (1), such that the calculation can implicitly include all orders of anharmonic scattering by MD simulations. From the results in Fig. 5, it appears that corresponding to the low-frequency band where the thermal conductivity difference is significant, the superlattice also exhibits PPR features that reflect the thermal conductivity difference, especially in the low frequency band at $3 \sim 10$ THz. As the phonon frequency increases from 1 THz to 10 THz, the PPR of the superlattice is invariably weakened to varying degrees. It is evident that at the trough of the weakened PPR, the different minima corresponding to the different superlattices also reflect the phonon activity and thus to some extent the relative magnitude of the thermal conductivity.

More importantly, thermal transport in solids can be understood in terms of a simple kinetic theory of gases, relying on the classical phonon gas model where the thermal conductivity of phonons can be expressed as:

$$\kappa = \frac{1}{3}C_V v_g \lambda \tag{4}$$

where C_V is the specific heat per unit volume of the particles, v_g is the phonon group velocity, and λ is the phonon mean free path (MFP) defined as the average distance traveled by the phonon between the occurrence of two scattering events. Next, we will go further to reveal the origin of the differential thermal conductivity in the Gr/C_3N superlattice in terms of intuitive phonon properties by means of the MFP and group velocity of phonons respectively.

In the phonon thermal transport of hybrid nano-systems, the phonon MFP reflects well the scattering of phonons during transport, which is decisive for the thermal conductivity of solids [47,48]. Due to the influence of the relative relationship between phonon MFP and system size on the phonon transport regime, under the NEMD approach, this can be achieved by Matthiessen's theorem $\frac{1}{\lambda(L)} = \frac{1}{\lambda} + \frac{1}{L}$ and the relation $\frac{\kappa_0}{\kappa(L)} = \frac{\lambda}{\lambda(L)}$ for the extrapolation of the thermal conductivity from finite to infinite system dimensions:

$$\begin{aligned}\frac{1}{\kappa(L)} &= \frac{1}{\kappa_0}\left(1+\frac{\lambda}{L}\right) \\ &= \frac{\lambda}{\kappa_0}\times\frac{1}{L}+\frac{1}{\kappa_0}\end{aligned} \tag{5}$$

where $\kappa(L)$ denotes the thermal conductivity of a finite system with feature size L and effective phonon MFP of $\lambda(L)$, and λ and κ_0 are the phonon MFP and thermal conductivity of an infinite size system, respectively. Also, with the help of the spectral thermal conductivities $\kappa(\omega)$ and $G(\omega)$ obtained by the HNEMD- and NEMD-based SHC methods, respectively, the phonon MFP can be extended to frequency-dependent results as follows:

$$\lambda = \frac{\kappa_0}{G_0}, \quad \lambda(\omega) \equiv \frac{\kappa_0(\omega)}{G_0(\omega)} = \frac{\kappa(\omega)}{G(\omega)} \tag{6}$$

Based on the above theory, we evaluate the phonon MFP information obtained for the Gr/C_3N lateral superlattice $G_1 \sim G_6$, as shown in Fig. 6. In terms of the overall phonon MFP, it clearly shows a decreasing and then increasing trend with increasing interface density in almost the same way as the thermal conductivity. Further refining to the frequency-dependent phonon MFP results, the maximum phonon MFP in the limit where ω tends to zero for the superlattice $G_1 \sim G_6$ is approximately 510 nm, 320 nm, 240 nm, 700 nm, 1600 nm, and 3770 nm, respectively, which does not appear to be in good agreement with the corresponding thermal conductivity results. However, as the phonon frequency increases to about 3 THz, the phonon MFP of the superlattices G_2 and G_3 start to produce a change in the ranking of the full superlattice results. The phonon MFP of G_2 exhibits a significant decrease and the magnitude relationship between the phonon MFP of the superlattices remains consistent with the thermal conductivity relationship in the low-and-mid frequency band where thermal transport is dominant. Similar to the spectral thermal conductivity

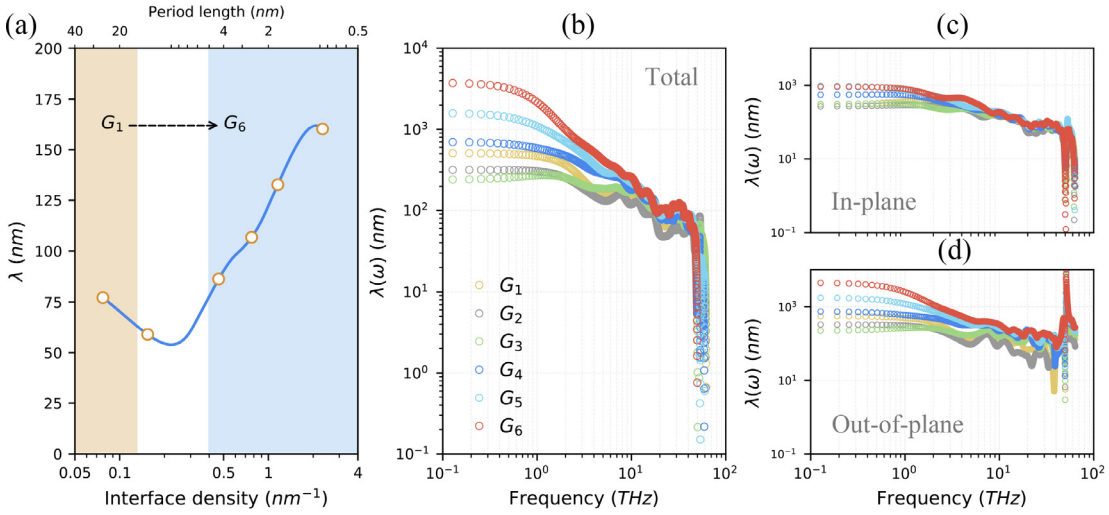

Fig. 6. (a) Variation of the phonon mean free path (MFP) of the Gr/C_3N superlattice $G_1 \sim G_6$ as a function of interface density and period length. The (b) spectral phonon MFP and its (c) in-plane and (d) out-of-plane components obtained by the SHC method are shown as a function of phonon frequency.

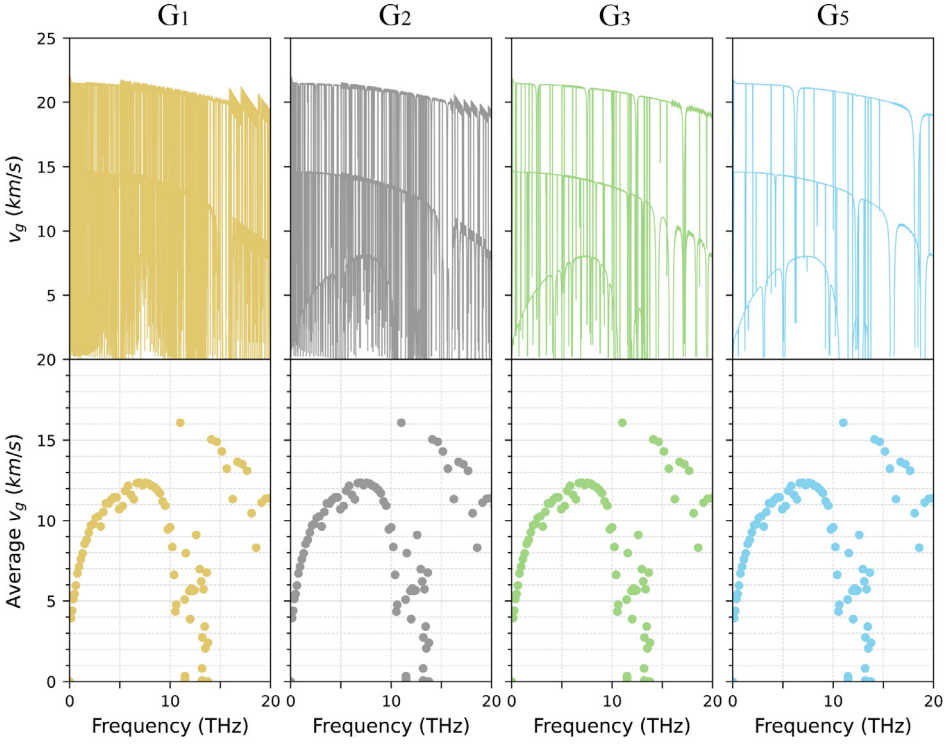

Fig. 7. The phonon group velocities v_g of representative structures G_1, G_2, G_3, and G_5 of the Gr/C_3N lateral superlattice and their averaging results obtained by sampling at intervals of 0.2 THz.

results, the difference in the in-plane component of the superlattice phonon MFP is also not significant. The phonon transport is clearly evident here: the increase in interface density appears to weaken the phonon MFP by enhancing scattering, but the smaller the period length the more phonons can be transported across the hetero-interfaces, and the phonon transport regime is then transformed from incoherent to coherent, reflecting the dual effects of the hetero-interface on the phonon thermal transport in the superlattice.

Finally, another important influence on the thermal conductivity in Eq. (4) will be considered, namely the phonon group velocity v_g, which reflects the propagation of energy by lattice vibrations [49]. For this purpose, we have selected four Gr/C_3N superlattices, G_1, G_2, G_3, and G_5, as representative structures and plotted their phonon dispersion in Fig. S9. Here, the low-frequency acoustic branch of the $0 \sim 20$ THz dominant thermal conductivity difference are only focused on. Note that here the number of atoms within the superlattice unit cell is high and proportional to the period length, and the number of vibration modes in the dispersion curves follows this pattern. In Fig. S9, the characteristic behaviour of the phonon dispersion curves for the four densely distributed superlattices is so similar that it is difficult to capture clear and valid information with the naked eye. Further, information on phonon group velocities was extracted from the above phonon dispersion relations and statistically better visualized average results were obtained, as shown in Fig. 7. It is not difficult to find that the difference in interface density in the direction of thermal transport across the hetero-interface in the Gr/C_3N superlattice

has almost no effect on the low-frequency phonon group velocity. Combined with the previous results, it can be concluded that the transformation of the phonon transport regime in the Gr/C_3N superlattice with changing interface density is all reflected in the change of phonon MFP, while the group velocity is almost unaffected.

4. Conclusion

In summary, through extensive MD simulations including HNEMD, NEMD and their respective spectral decomposition methods, complemented by a mechanistic analysis of the lattice dynamics at the phonon perspective, we have investigated in depth the phonon thermal transport behavior across the hetero-interface in the lateral superlattice. As the hetero-interface density increases, the thermal conductivity of the superlattice shows a parabolic trend of decreasing and then increasing, which implies a shift of the phonon transport from incoherent to coherent regimes. The decomposition of the in-plane and out-of-plane contributions to the thermal conductivity and the phonon frequency dependence analysis reveal that, as in the case of the universal phonon thermal transport regime, it is the low-frequency out-of-plane phonons that dominate the difference in thermal conductivity of the different Gr/C_3N superlattices. The comparative analysis and the associated phonon calculations with the introduction of random superlattices together show that: (i) the stronger phonon scattering due to the increased density of the hetero-interface continuously weakens the thermal conductivity, which corresponds mainly to the difference between the superlattices in the incoherent transport regime and the random superlattices in the whole regime; (ii) while the increase of the superlattice interface density in general leads to a significant increase of the phonon MFP and thus of the thermal conductivity after entering the coherent transport domain, and the phonon MFP is the only factor in the increase of the thermal conductivity, independent of the phonon group velocity. This can be attributed qualitatively to the dual effects of increasing of the hetero-interface density, or decreasing the period length, on phonon thermal transport, which on the one hand weakens the thermal conductivity by enhancing phonon scattering, and on the other hand increases the thermal conductivity by reducing the barriers to phonon transport across the interface. It is this combination of factors that leads to the interesting trends in the thermal conductivity of superlattices. These findings provide a new understanding of the mechanism of the influence of hetero-interfaces on phonon thermal transport in 2D lateral superlattices, which is expected to further advance the development of superlattice nanodevices for optimal thermal management and design.

Declaration of Competing Interest

Authors declare that they have no conflict of interest.

CRediT authorship contribution statement

Xin Wu: Conceptualization, Formal analysis, Investigation, Methodology, Software, Validation, Visualization, Writing – original draft, Writing – review & editing. **Penghua Ying:** Formal analysis, Methodology, Software, Writing – original draft. **Chunlei Li:** Funding acquisition, Project administration, Resources. **Qiang Han:** Funding acquisition, Project administration, Resources, Supervision.

Data availability

Data will be made available on request.

Acknowledgments

The authors are grateful for support from the National Natural Science Foundation of China (11972160), Guangdong Basic and Applied Basic Research Foundation (2019A1515011900), Science and Technology Program of Guangzhou, China (202002030367).

Supplementary material

Supplementary material associated with this article can be found, in the online version, at doi:10.1016/j.ijheatmasstransfer.2022.123643.

References

[1] R. Fu, Y. Xu, Y. Liu, Y. Lin, K. Xu, Y. Chang, Y. Fu, Z. Zhang, J. Wu, Thermally induced hex-graphene transitions in 2Dcarbon crystals, Nanotech. Rev. 11 (1) (2022) 1101–1114.
[2] J. Liu, P. Šesták, Z. Zhang, J. Wu, Brittle and ductile behavior in monolayer MoS_2, Mater. Today Nano 20 (2022) 100245.
[3] H. Yu, K. Xu, Z. Zhang, X. Cao, J. Weng, J. Wu, Oxygen functionalization-induced crossover in the tensile properties of the thinnest 2D Ti_2C mxene, J. Mater. Chem. C 9 (7) (2021) 2416–2425.
[4] Y. Xu, Q. Shi, Z. Zhou, K. Xu, Y. Lin, Y. Li, Z. Zhang, J. Wu, Machine learning assisted insights into the mechanical strength of nanocrystalline graphene oxide, 2D Mater. 9 (3) (2022) 035002.
[5] M.M. Waldrop, The chips are down for Moore's law, Nature 530 (7589) (2016) 144–147.
[6] X.K. Chen, K.Q. Chen, Thermal transport of carbon nanomaterials, J. Phys. Condens. Matter 32 (15) (2020) 153002.
[7] M. An, H. Wang, Y. Yuan, D. Chen, W. Ma, S.W. Sharshir, Z. Zheng, Y. Zhao, X. Zhang, Strong phonon coupling induces low thermal conductivity of one-dimensional carbon boron nanotube, Surf. Interfaces 28 (2022) 101690.
[8] T. Miao, M. Xiang, D. Chen, M. An, W. Ma, Thermal transport characteristics of two-dimensional t-$PdTe_2$ and its janus structures, Int. J. Heat Mass Transf. 183 (2022) 122099.
[9] Y. Zhang, M. An, D. Song, A. Fan, D. Chen, H. Wang, W. Ma, X. Zhang, Phonon magic angle in two-dimensional puckered homostructures, J. Mater. Chem. C 9 (37) (2021) 12741–12750.
[10] Z. Zhang, Y. Guo, M. Bescond, J. Chen, M. Nomura, S. Volz, Coherent thermal transport in nano-phononic crystals: an overview, APL Mater. 9 (8) (2021) 081102.
[11] M. Nomura, R. Anufriev, Z.W. Zhang, J. Maire, Y.Y. Guo, R. Yanagisawa, S. Volz, Review of thermal transport in phononic crystals, Mater. Today Phys. 22 (2022) 100613.
[12] X.K. Chen, X.Y. Hu, P. Jia, Z.X. Xie, J. Liu, Tunable anisotropic thermal transport in porous carbon foams: the role of phonon coupling, Int. J. Mech. Sci. 206 (2021) 106576.
[13] H. Wang, Y. Cheng, Z. Fan, Y. Guo, Z. Zhang, M. Bescond, M. Nomura, T. Ala-Nissila, S. Volz, S. Xiong, Anomalous thermal conductivity enhancement in low dimensional resonant nanostructures due to imperfections, Nanoscale 13 (22) (2021) 10010–10015.
[14] K. Li, Y. Cheng, H. Wang, Y. Guo, Z. Zhang, M. Bescond, M. Nomura, S. Volz, X. Zhang, S. Xiong, Phonon resonant effect in silicon membranes with different crystallographic orientations, Int. J. Heat Mass Transf. 183 (2022) 122144.
[15] V. Narayanamurti, H.L. Störmer, M.A. Chin, A.C. Gossard, W. Wiegmann, Selective transmission of high-frequency phonons by a superlattice: the "dielectric" phonon filter, Phys. Rev. Lett. 43 (27) (1979) 2012–2016.
[16] C. Dames, G. Chen, Theoretical phonon thermal conductivity of Si/Ge superlattice nanowires, J. Appl. Phys. 95 (2) (2004) 682–693.
[17] M. Hu, D. Poulikakos, Si/Ge superlattice nanowires with ultralow thermal conductivity, Nano Lett. 12 (11) (2012) 5487–5494.
[18] Y. Guo, M. Bescond, Z. Zhang, S. Xiong, K. Hirakawa, M. Nomura, S. Volz, Thermal conductivity minimum of graded superlattices due to phonon localization, APL Mater. 9 (9) (2021) 091104.
[19] S. Xiong, B. Latour, Y. Ni, S. Volz, Y. Chalopin, Efficient phonon blocking in sic antiphase superlattice nanowires, Phys. Rev. B 91 (22) (2015) 224307.
[20] K. Xu, T. Liang, Y. Fu, Z. Wang, Z. Fan, N. Wei, J. Xu, Z. Zhang, J. Wu, Gradient nano-grained graphene as 2D thermal rectifier: a molecular dynamics based machine learning study, Appl. Phys. Lett. 121 (13) (2022) 133501.
[21] Y. Zhang, Q. Lv, H. Wang, S. Zhao, Q. Xiong, R. Lv, X. Zhang, Simultaneous electrical and thermal rectification in a monolayer lateral heterojunction, Science 378 (2022) 169–175.
[22] K. Xu, T. Liang, Z. Zhang, X. Cao, M. Han, N. Wei, J. Wu, Grain boundary and misorientation angle-dependent thermal transport in single-layer MoS_2, Nanoscale 14 (4) (2022) 1241–1249.
[23] I.M. Felix, L.F.C. Pereira, Thermal conductivity of graphene-hBN superlattice ribbons, Sci. Rep. 8 (1) (2018) 2737.
[24] M.N. Luckyanova, J. Garg, K. Esfarjani, A. Jandl, M.T. Bulsara, A.J. Schmidt, A.J. Minnich, S. Chen, M.S. Dresselhaus, Z. Ren, E.A. Fitzgerald, G. Chen, Coherent phonon heat conduction in superlattices, Science 338 (6109) (2012) 936–939.

[25] X. Wu, Q. Han, Transition from incoherent to coherent phonon thermal transport across graphene/h-BN van der Waals superlattices, Int. J. Heat Mass Transf. 184 (2022) 122390.
[26] M. An, D.S. Chen, W.G. Ma, S.Q. Hu, X. Zhang, Directly visualizing the crossover from incoherent to coherent phonons in two-dimensional periodic MoS_2/$MoSe_2$ arrayed heterostructure, Int. J. Heat Mass Transf. 178 (2021) 121630.
[27] J. Mahmood, E.K. Lee, M. Jung, D. Shin, H.J. Choi, J.M. Seo, S.M. Jung, D. Kim, F. Li, M.S. Lah, N. Park, H.J. Shin, J.H. Oh, J.B. Baek, Two-dimensional polyaniline (C_3N) from carbonized organic single crystals in solid state, Proc. Natl. Acad. Sci. 113 (27) (2016) 7414–7419.
[28] T. Zhang, H. Qi, Z. Liao, Y.D. Horev, L.A. Panes-Ruiz, P.S. Petkov, Z. Zhang, R. Shivhare, P. Zhang, K. Liu, V. Bezugly, S. Liu, Z. Zheng, S. Mannsfeld, T. Heine, G. Cuniberti, H. Haick, E. Zschech, U. Kaiser, R. Dong, X. Feng, Engineering crystalline quasi-two-dimensional polyaniline thin film with enhanced electrical and chemiresistive sensing performances, Nat. Commun. 10 (1) (2019) 4225.
[29] M. An, L. Li, S. Hu, Z. Ding, X. Yu, B. Demir, N. Yang, W. Ma, X. Zhang, Mass difference and polarization lead to low thermal conductivity of graphene-like carbon nitride (C_3N), Carbon 162 (2020) 202–208.
[30] K. Einalipour Eshkalak, S. Sadeghzadeh, F. Molaei, Interfacial thermal resistance mechanism for the polyaniline (C_3N)-graphene heterostructure, J. Phys. Chem. C 124 (26) (2020) 14316–14326.
[31] J. Song, Z. Xu, X. He, Thermal energy transport across the graphene/C_3N interface, Int. J. Heat Mass Transf. 157 (2020) 119954.
[32] X. Wu, Q. Han, Semidefective graphene/h-BN in-plane heterostructures: enhancing interface thermal conductance by topological defects, J. Phys. Chem. C 125 (4) (2021) 2748–2760.
[33] T. Liang, M. Zhou, P. Zhang, P. Yuan, D. Yang, Multilayer in-plane graphene/hexagonal boron nitride heterostructures: insights into the interfacial thermal transport properties, Int. J. Heat Mass Transf. 151 (2020) 119395.
[34] B. Liu, J.A. Baimova, C.D. Reddy, S.V. Dmitriev, W.K. Law, X.Q. Feng, K. Zhou, Interface thermal conductance and rectification in hybrid graphene/silicene monolayer, Carbon 79 (2014) 236–244.
[35] Z. Fan, L.F.C. Pereira, H.-Q. Wang, J.-C. Zheng, D. Donadio, A. Harju, Force and heat current formulas for many-body potentials in molecular dynamics simulations with applications to thermal conductivity calculations, Phys. Rev. B 92 (9) (2015) 094301.
[36] Z. Fan, L.F.C. Pereira, P. Hirvonen, M.M. Ervasti, K.R. Elder, D. Donadio, T. Ala-Nissila, A. Harju, Thermal conductivity decomposition in two-dimensional materials: application to graphene, Phys. Rev. B 95 (14) (2017) 144309.
[37] Z.Y. Fan, W. Chen, V. Vierimaa, A. Harju, Efficient molecular dynamics simulations with many-body potentials on graphics processing units, Comput. Phys. Commun. 218 (2017) 10–16.
[38] Z. Fan, Y. Wang, P. Ying, K. Song, J. Wang, Y. Wang, Z. Zeng, K. Xu, E. Lindgren, J.M. Rahm, A.J. Gabourie, J. Liu, H. Dong, J. Wu, Y. Chen, Z. Zhong, J. Sun, P. Erhart, Y. Su, T. Ala-Nissila, GPUMD: a package for constructing accurate machine-learned potentials and performing highly efficient atomistic simulations, J. Chem. Phys. 157 (2022) 114801.
[39] L. Lindsay, D.A. Broido, Optimized Tersoff and Brenner empirical potential parameters for lattice dynamics and phonon thermal transport in carbon nanotubes and graphene, Phys. Rev. B 81 (20) (2010).
[40] A. Kinaci, J.B. Haskins, C. Sevik, T. Çağin, Thermal conductivity of BN-C nanostructures, Phys. Rev. B 86 (11) (2012) 115410.
[41] Z. Li, S. Xiong, C. Sievers, Y. Hu, Z. Fan, N. Wei, H. Bao, S. Chen, D. Donadio, T. Ala-Nissila, Influence of thermostatting on nonequilibrium molecular dynamics simulations of heat conduction in solids, J. Chem. Phys. 151 (23) (2019).
[42] J. Chen, G. Zhang, B. Li, Molecular dynamics simulations of heat conduction in nanostructures: effect of heat bath, J. Phys. Soc. Jpn. 79 (7) (2010) 074604.
[43] X. Wu, Q. Han, Thermal transport in pristine and defective two-dimensional polyaniline (C_3N), Int. J. Heat Mass Transf. 173 (2021) 121235.
[44] Z. Fan, H. Dong, A. Harju, T. Ala-Nissila, Homogeneous nonequilibrium molecular dynamics method for heat transport and spectral decomposition with many-body potentials, Phys. Rev. B 99 (6) (2019) 064308.
[45] X.-K. Chen, J.-L. Tan, M. Pang, Z.-X. Xie, W.-X. Zhou, J. Liu, Interlayer coupling-induced controllable negative differential thermal resistance in graphene/h-BN van der Waals heterostructure, Appl. Phys. Lett. 121 (14) (2022) 142203.
[46] H. Matsubara, D. Surblys, Y. Bao, T. Ohara, Molecular dynamics study on vibration-mode matching in surfactant-mediated thermal transport at solid-liquid interfaces 347, 118363.
[47] K. Sääskilahti, J. Oksanen, J. Tulkki, S. Volz, Role of anharmonic phonon scattering in the spectrally decomposed thermal conductance at planar interfaces, Phys. Rev. B 90 (13) (2014) 134312.
[48] K. Sääskilahti, J. Oksanen, S. Volz, J. Tulkki, Frequency-dependent phonon mean free path in carbon nanotubes from nonequilibrium molecular dynamics, Phys. Rev. B 91 (11) (2015) 115426.
[49] P. Ying, T. Liang, Y. Du, J. Zhang, X. Zeng, Z. Zhong, Thermal transport in planar sp2-hybridized carbon allotropes: a comparative study of biphenylene network, pentaheptite and graphene, Int. J. Heat Mass Tran. 183 (2022) 122060.